batteries

MDPI

Article

High Areal Capacity and Sustainable High Energy in Ferroelectric Doped Holey Graphene/Sulfur Composite Cathode for Lithium-Sulfur Batteries

Claudia C. Zuluaga-Gómez [1,*], Balram Tripathi [1], Christian O. Plaza-Rivera [2], Rajesh K. Katiyar [1], Margarita Correa [3], Dhiren K. Pradhan [4], Gerardo Morell [1] and Ram S. Katiyar [1,*]

[1] Department of Physics, University of Puerto Rico at Río Piedras, San Juan, PR 00925-2537, USA
[2] Department of Physics, University of Puerto Rico at Mayagüez, Mayagüez, PR 00682, USA
[3] Grupo Física de Materiales, Universidad del Atlántico, Puerto Colombia 081001, Colombia
[4] Department of Materials Science & Engineering, University of Tennessee, Knoxville, TN 37996, USA
* Correspondence: claudia.zuluaga@upr.edu (C.C.Z.-G.); ram.katiyar@upr.edu (R.S.K.)

Abstract: In this study, we are reporting the impact of the incorporation of ferroelectric nanoparticles (FNPs), such as $BaTiO_3$ (BTO), $BiFeO_3$ (BFO), $Bi_4NdTi_3Fe_{0.7}Ni_{0.3}O_{15}$ (BNTFN), and $Bi_4NdTi_3Fe_{0.5}Co_{0.5}O_{15}$ (BNTFC), as well as the mass loading of sulfur to fabricated solvent-free sulfur/holey graphene-carbon black/polyvinylidene fluoride (S/FNPs/CBhG/PVDF) composite electrodes to achieve high areal capacity for lithium-sulfur (Li-S) batteries. The dry-press method was adopted to fabricate composite cathodes. The hG, a conductive and lightweight scaffold derived from graphene, served as a matrix to host sulfur and FNPs for the fabrication of solvent-free composites. Raman spectra confirmed the dominant hG framework for all the composites, with strong D, G, and 2D bands. The surface morphology of the fabricated cathode system showed a homogeneous distribution of FNPs throughout the composites, confirmed by the EDAX spectra. The observed Li^+ ion diffusion coefficient for the composite cathode started at 2.17×10^{-16} cm^2/s ($S_{25}(CBhG)_{65}PVDF_{10}$) and reached up to the highest value (4.15×10^{-15} cm^2/s) for $S_{25}BNTFC_5(CBhG)_{60}PVDF_{10}$. The best discharge capacity values for the $S_{25}(CBhG)_{65}PVDF_{10}$ and $S_{25}BNTFC_5(CBhG)_{60}PVDF_{10}$ composites started at 1123 mAh/g_s and 1509 mAh/g_s and dropped to 612 mAh/g_s and 572 mAh/g_s, respectively, after 100 cycles; similar behavior was exhibited by the other composites that were among the best. These are better values than those previously reported in the literature. The incorporation of ferroelectric nanoparticles in the cathodes of Li-S batteries reduced the rapid formation of polysulfides due to their internal electric fields. The areal capacity for the $S_{25}(CBhG)_{65}PVDF_{10}$ composites was 4.84 mAh/cm^2 with a mass loading of 4.31 mg_s/cm^2, while that for the $S_{25}BNTFC_5(CBhG)_{60}PVDF_{10}$ composites was 6.74 mAh/cm^2 with a mass loading of 4.46 mg_s/cm^2. It was confirmed that effective FNP incorporation within the S cathode improves the cycling response and stability of cathodes, enabling the high performance of Li-S batteries.

Keywords: polysulfides; ferroelectric nanoparticles; holey graphene; lithium-sulfur batteries

check for updates

Citation: Zuluaga-Gómez, C.C.; Tripathi, B.; Plaza-Rivera, C.O.; Katiyar, R.K.; Correa, M.; Pradhan, D.K.; Morell, G.; Katiyar, R.S. High Areal Capacity and Sustainable High Energy in Ferroelectric Doped Holey Graphene/Sulfur Composite Cathode for Lithium-Sulfur Batteries. *Batteries* **2023**, *9*, 293. https://doi.org/10.3390/batteries9060293

Academic Editor: Sang Bok Lee

Received: 25 April 2023
Revised: 18 May 2023
Accepted: 24 May 2023
Published: 26 May 2023

1. Introduction

Li-S rechargeable batteries with high-energy capacity are considered one of the most promising energy storage systems for electronic devices and electric vehicles [1]. These Li-S batteries have the following advantages: low cost, low operating voltage (2.2 V), environmentally friendly, good energy storage system due to their higher theoretical energy density (2600 Wh/kg), and theoretical specific capacity (1675 mAh/g) [2–6]. On the other hand, Li-S batteries present a disadvantage since they possess low cyclability [7]. These challenges can be dealt with by adding a carrier material with a rich pore structure to adsorb lithium polysulfides and chemisorption [8,9], limiting the dissolution and diffusion of lithium polysulfide between polar carrier materials and lithium polysulfides

(LiPs) [10]. The insulating nature of sulfur still limits the development of high-loading sulfur cathodes with sufficient sulfur content, and most existing cathodes have low sulfur loadings (<2 mg/cm^2) and contents (<60 wt%) [11]. To address these problems, porous substrates with various functions have emerged as effective sulfur hosts that can prevent the rapid loss of large amounts of polysulfides, especially at increased sulfur loadings. To improve the sulfur conductivity and loading area, porous carbon materials are applied. The pore structure enhances sulfur loading and promotes fast ion diffusion. Furthermore, the capillary effect of the elemental sulfur-filled pores can effectively inhibit the diffusion of LiPs into the electrolyte, slow down the shuttle effect, and increase the utilization rate of active materials to improve the energy density of Li-S batteries. Various synthesis strategies of S-doped carbon as electrode materials for energy storage applications have been reported [12], including thermal treatment [13], hydrothermal methods [14], biomass-assisted synthesis [15], polymer-assisted synthesis [16], template-assisted synthesis [17], microwave-assisted synthesis [18], solvothermal methods [19], sol-gel processing [20], chemical vapor deposition [21], and sublimation [22]. Song and coworkers [23] synthesized highly crumpled nitrogen-doped graphene (NG) with an ultrahigh pore volume and large surface area, enabling strong LiPs adsorption and high sulfur content and areal loading in the NG host; they reported a high capacity of ≈1000 mAh/g with 80 wt% sulfur content and a high sulfur loading of 5 mg/cm^2. Ferroelectric nanoparticles (FNPs) exhibiting spontaneous polarization provide strong interactions with electric fields [24], having the ability to suppress shuttle effects in sulfur cathodes. FNPs in cathodes eliminate the concentration gradient of Li-ions near the deposition surface, yielding diffusion pathways in electrolyte/active material and accelerating the transfer speed of Li-ions. In commercial batteries, the areal capacity density of cathodes is generally higher than 2.0 mAh/cm^2, with an average output voltage of 3.5 V. However, the areal capacity density of sulfur cathodes is higher than 3.3 mAh/cm^2, considering the average voltage of 2.1 V for Li-S batteries [25]. Moreover, for electric vehicle (EV) applications, to deliver a mileage of more than 300 miles, an aerial capacity of 5 mAh/cm^2 and energy density of 500 Wh/kg are required to support their practical power output requirements, due to which high sulfur loading and utilization are needed to achieve the high areal capacity and high energy density of Li-S batteries [26,27]. We recently demonstrated that the hG framework greatly improves the performance of electrodes, facilitating the active material to fully participate in electrochemical reactions [28]. Ferroelectrics have strong polarization and can assist polysulfides chemisorption and alter Li$^+$ diffusion. The uniform distribution of ferroelectrics is expected to contribute to enhanced affinity to polysulfides in the overall cell system [29,30]. Moreover, the C/S + BTO composite exhibits a higher initial discharge capacity of 1143 mAh/g at 0.2 C after 100 cycles; for the C/S electrode without BTO nanoparticles, a discharge capacity of 407 mAh/g can be obtained after 100 cycles [31]. In 2019, a unique "black" B-BTO was developed for the first time as a multifunctional sulfur immobilizer to improve performance and facilitate high conductivity with electron transfer and kinetics with sulfur reaction in this type of battery [32]. The bismuth ferrite $BiFeO_3$ (BFO) incorporated into cathodes reduced the impact of polysulfide shuttle and improved cyclic stability. The cathode capacity of the $S_{60}BFO_{30}C_{10}$ composite Li-S battery reached ~1600 mAh/g, and the cell operated for up to 30 cycles [33]. In most studies of Li-S batteries, the ferroelectric nanoparticle materials were incorporated into the separator or cathode of devices. In Table 1, we make a comparison between these studies and our work in terms of capacity retention, cyclability, initial specific capacity, and Coulombic efficiency [29,31–35]. We achieved a much better overall performance in relation to these studies. In this study, we are presenting the effect of the mass loading and coupling of different FNPs such as BTO, BFO, BNTFN, and BNTFC on hG/S composites to achieve high areal capacity in Li-S cathodes.

Table 1. Comparison of reported results on incorporated ferroelectric materials in Li-S batteries regarding initial specific capacity, cyclability, capacity retention, and Coulombic efficiency of separator and cathode compositions.

Reference	Preparation Method	Incorporated Ferroelectric Materials	Initial Specifics Capacity [mAh/g]	Cyclability	Capacity Retention	Coulombic Efficiency
2016 [29] Separator	Were dispersed in acetone (80 mL) using a high-speed mixer (Primix) at room temperature for 2 hrs	A. PE B. PE-poled BTO C. PE–BTO	997.2 1121.1 1124	50 cycles 50 cycles 50 cycles	59.4% 82.8% 72.3%	26.3% 79.6% 42.3%
2016 [31] Cathodes	Slurry	A. C/S B. C/S + BTO C. Multi-rate (A and B)	407 1143-0.2 C A. B.	100 cycles 100 cycles 60 cycles	——— ——— ———	——— ——— ———
2019 [32] Cathodes	Slurry	A. C/S B. C/S@B-BTO C. C/S@W-BTO D. Multi-rate (A, B, and C)	1009.1 1129.5 928.2 A. 223.9, B. 607.6 C. 475.2	200 cycles 200 cycles 200 cycles 50 cycles 50 cycles 50 cycles	71.3% 80.2% 42.5% ——— ——— ———	——— ——— ——— ——— ——— ———
2021 [34]	Separator	A. Celgard 2320 B. AC/GO C. AC/BTO D. AC/BTO-g-GO C. Multi-rate (B, C, and D)	910 1200 950 1450-0.1 C ———	——— ——— ——— 100 cycles 55 cycles	——— ——— ——— ——— ———	——— ——— ——— ——— 75%
2021 [33] Cathodes	Slurry	A. S60BFO30C10 B. S70BFO20C10 C. S80BFO10C10	1600 1525 1450	30 cycles 30 cycles 30 cycles	~86% ~62%	86% ———
2023 [35] Cathodes	Dry pressable	A. S/hG B. S/BFO/hG C. S/BTO/hG D. S/BNTFN/hG E. S/BNTFC/hG	1390 1316 1409 1069 1330	6 cycles 57 cycles 58 cycles 18 cycles 37 cycles	57.7% 26% 34% 90% 53%	25% 83.71% 82.65% 78.93% 86.92%
2023 This work Cathodes	Dry pressable	A. S/CBhG/PVDF B. S/BTO/CBhG/PVDF C. S/BFO/CBhG/PVDF D. S/BNTFN/CBhG/PVDF E. S/BNTFC/CBhG/PVDF	1123 1402 1430 1486 1509	134 cycles 110 cycles 116 cycles 158 cycles 107 cycles	54.49% 46.72% 45.31% 43.40% 37.90%	83% 87% 78% 93% 90%

2. Materials, Methods, and Characterizations

Materials. In this work, the hG was prepared from graphene (Vorbeck materials) using the established one-step air oxidation procedure previously reported [36]. Bis(trifluoromethylsulfonyl)imide lithium salt (LiTFSI; 98+%), lithium nitrate ($LiNO_3$; 99.99%), 1,2-dimethoxyethane (DME; 99+%), and 1,3-dioxolane (DOL; 99.5%) were purchased from Thermo Fisher (Waltham, MA, USA) * (* Specific vendor and manufacturer names do not imply an endorsement by the authors, nor does it imply that the specified material or equipment is the best available.). Sulfur (S; 99.998%), highly pure barium carbonate ($BaCO_3$; 99.8%), neo-dymium (III) oxide (Nd_2O_3; 99.9%), lithium foil (0.75 mm thick × 19 mm wide) (Al; 99.9%), high-purity cobalt (II, III) oxide (Co_3O_4; 99.998%), polyvinylidene fluoride (PVDF), and carbon back (CB) were purchased from Alfa Aesar (Haverhill, MA, USA) * (* Specific vendor and manufacturer names do not imply an endorsement by the authors, nor does it imply that the specified material or equipment is the best available.). Iron oxide (Fe_2O_3; 99.998%), nickel (III) oxide nanopowder (Ni_2O_3; 99%), and Celgard membrane (25 µm thickness and 85 mm width) were purchased from Sigma-Aldrich (St. Louis, MO, USA) * (* Specific vendor and manufacturer names do not imply an endorsement by the authors, nor does it imply that the specified material or equipment is the best available.). High-purity bismuth oxide (Bi_2O_3; 99.9%) was purchased from Fluka and titanium dioxide

(TiO_2; 97%) was purchased from Fisher Scientific * (* Specific vendor and manufacturer names do not imply an endorsement by the authors, nor does it imply that the specified material or equipment is the best available). All precursors and elements for the battery assembly were used inside the glove box with argon-filled water (H_2O) and oxygen (O_2) contents < 0.5 ppm.

Synthesis of ferroelectric nanoparticles. The FNPs were synthesized via mechanical activation followed by thermal treatment. Stoichiometric amounts of 15 wt% excess of Bi_2O_3 were used to compensate for volatilization loss during the thermal treatment. The oxides were mixed with isopropanol using a high-energy ball-milling planetary machine with zirconia balls (Across International, PQ-N04 Planetary Ball Mill, San Juan, PR, USA) operating at 45 Hz (2700 rpm) for 8 hrs. The synthesized material was dried on a hot plate at 100 °C for 8 hrs. We used a furnace (Carbolite, HTF1700, San Juan, PR, USA) at a heating and cooling rate of 5 °C/min in which the powders were calcined.

Sulfur-FNPs-holey graphene/carbon black-PVDF composite cathode preparation and characterizations. In a typical experiment to prepare $S_{25}(CBhG)_{65}PVDF_{10}$ and $S_{25}FNPs_5(CB_{98.5\%}hG_{1.5\%})_{60}PVDF_{10}$ composite cathodes, individual powder was mixed in a particular ratio by using ball milling to fabricate composite electrodes of $S_{25}(CB_{98.5\%}hG_{1.5\%})_{65}PVDF_{10}$ and $S_{25}FNPs_5(CB_{98.5\%}hG_{1.5\%})_{60}PVDF_{10}$. For each sample, a 100 mg composite was prepared in the desirable amount of S, CBhG, FNP, and PVDF powders (weight ratios of 2.5:0.0:6.5:1.0 and 2.5:0.5:6.0:1.0 for a total of five different samples) and loaded in a 50 mL zirconia vial. After placing two zirconia balls in the vial, the set was secured in PQ-N04 series planetary ball mills and milled for 10–15 s to yield the $S_{25}(CBhG)_{65}PVDF_{10}$ and $S_{25}FNPs_5(CB_{98.5\%}hG_{1.5\%})_{60}PVDF_{10}$ composites. The PVDF was used as a binder and the d CB was used as a conductor to improve the electrical conductivity and cycle life of the active material. PVDF as a binder helps counter volumetric changes occurring in the insertion electrodes during intercalation/deintercalation and ensures adhesion to the current collectors, which is useful for the stability of the electrodes. The fabrication of composite cathodes using the dry-press method is facile and does not require the use of solvents. The hG can be compressed from its dry powder form into solid architectures of various shapes [37–39]. For the fabrication of the electrode disc, 20 mg of the material was added to a 13 mm diameter stainless-steel pressing die. The pressed powders were directly used as the composite cathodes $S_{25}(CBhG)_{65}PVDF_{10}$ and $S_{25}FNPs_5(CBhG)_{60}PVDF_{10}$, while the polypropylene membrane was used as a separator and lithium foil was used as an anode for assembling the coin cells (CR2032). To prepare the electrolyte, 1 M of LiTFSI and 0.2 M of $LiNO_3$ were dissolved in DOL/DME (1:1, v/v). To calculate the proper amount of electrolyte (40 uL), we used 5.72 mg_s of the active mass with cathode loadings of 7 mL/g_s. This technique facilitates preparation, and it is less time-consuming than conventional solvent-based methods. Table 2 summarizes the critical cell parameters, such as sulfur content, sulfur loading, and electrolyte-to-sulfur ratios. A powder X-ray diffractometer was used for structure, scanning electron microscopy was used for the surface morphology of the electrodes, Raman spectroscopy was performed for the electronic structure, and galvanostatic discharge-charge curves were collected using a battery tester. A detailed description of FNP synthesis and intercalation inside a sulfur cathode and FNP characterization was provided in the article "Holey Graphene/Ferroelectric/Sulfur Composite Cathodes for High-Capacity Lithium-Sulfur Batteries", published in ACS Omega by the authors [35].

Table 2. Critical cell parameters.

Electrodes	Sulfur Content (wt%) [mg_s]	Sulfur Loading [mg_s/cm^2]	Electrolyte-to-Sulfur Ratio [µL]
$\mathbf{S_{25}(CBhG)_{65}PVDF_{10}}$	5.72	4.31	40
$\mathbf{S_{25}BTO_5(CBhG)_{60}PVDF_{10}}$	4.81	3.62	34
$\mathbf{S_{25}BFO_5(CBhG)_{60}PVDF_{10}}$	5.20	3.92	36
$\mathbf{S_{25}BNTFN_5(CBhG)_{60}PVDF_{10}}$	4.57	3.45	32
$\mathbf{S_{25}BNTFCO_5(CBhG)_{60}PVDF_{10}}$	5.92	4.46	42

3. Results and Discussion

Figure 1a–e shows the X-ray diffraction (XRD) spectra of the $S_{25}(CBhG)_{65}PVDF_{10}$ and $S_{25}FNPs_5(CBhG)_{60}PVDF_{10}$ composites. The XRD analysis was performed to investigate structural changes due to the incorporation of materials such as BTO [37], BFO [40], BNTFN [41], and BNTFC [42] and their possible reactions with S, CB, hG, and PVDF. As shown in Figure 1, the prominent peak of *hkl* (222) at 2θ = 23° corresponded to the *Fddd* orthorhombic structure of S (JCPDS no. 08-0247) [43,44]. The peak planes of (002) and (101) were at 2θ = 25° and 43° (attributed to carbon materials CB or hG), respectively; however, the (110) plane at 2θ = 27° corresponded to PVDF. These peaks were detected in all cathode compounds demonstrating the presence of all the aforementioned materials. Furthermore, the rest of the identified peaks could be perfectly indexed with their respective miller indices in the XRD spectra corresponding to the FNPs.

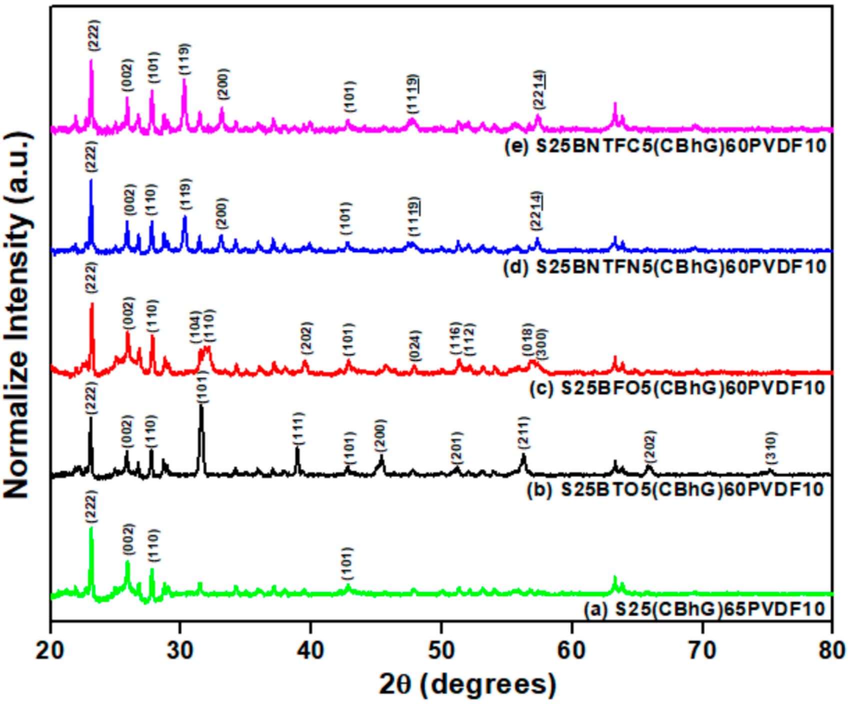

Figure 1. XRD spectra of (**a**) $S_{25}(CBhG)_{65}PVDF_{10}$, (**b**) $S_{25}BTO_5(CBhG)_{60}PVDF_{10}$, (**c**) $S_{25}BFO_5(CBhG)_{60}PVDF_{10}$, (**d**) $S_{25}BNTFN_5(CBhG)_{60}PVDF_{10}$, and (**e**) $S_{25}BNTFC_5(CBhG)_{60}PVDF_{10}$ composites.

Figure 2a–e shows the Raman spectra for the $S_{25}(CBhG)_{65}PVDF_{10}$ and $S_{25}FNPs_5(CBhG)_{60}$-$PVDF_{10}$ composites. The pronounced D band (disorder-induced phonon mode) at approximately 1336 cm^{-1} and G band (associated with in-plane vibration of the graphite lattice) at approximately 1575 cm^{-1} suggest a graphite-like carbon framework [45,46]. The intensity ratios (I_D/I_G) shown in Figure 2a (I_D/I_G was 1.06 for S/CBhG/PVDF), Figure 2b (I_D/I_G was 1.10 for S/BTO/CBhG/PVDF), Figure 2c (I_D/I_G was 1.01 for S/BFO/CBhG/PVDF), Figure 2e (I_D/I_G was 1.00 for S/BNTFC/CBhG/PVDF), and Figure 2d (I_D/I_G was 0.97 for S/BNTFN/CBhG/PVDF) were slightly reduced, presumably due to defect removal through the combined effects of ferroelectric nanoparticles doping. The Raman peaks for 2D and D + G were also visible at approximately 2700 cm^{-1}, this was attributed to the layered structure of the graphene.

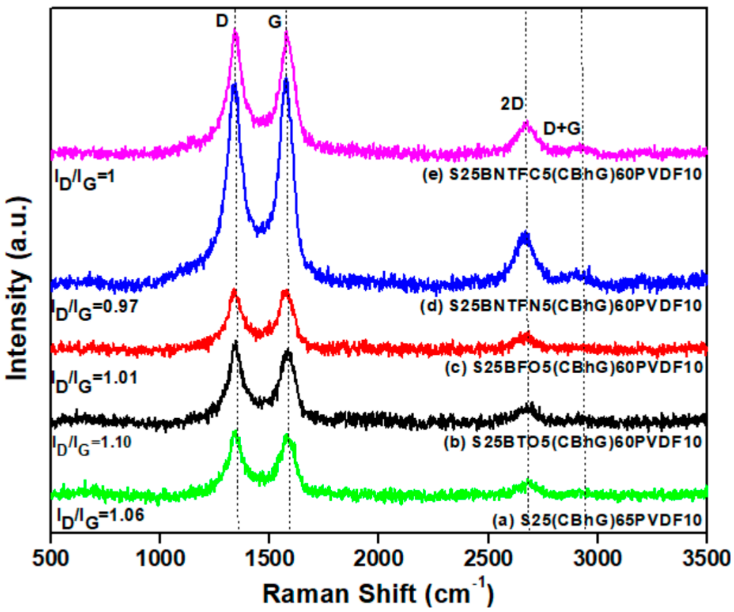

Figure 2. Raman spectra of (**a**) $S_{25}(CBhG)_{65}PVDF_{10}$, (**b**) $S_{25}BTO_5(CBhG)_{60}PVDF_{10}$, (**c**) $S_{25}BFO_5(CBhG)_{60}PVDF_{10}$, (**d**) $S_{25}BNTFN_5(CBhG)_{60}PVDF_{10}$, and (**e**) $S_{25}BNTFC_5(CBhG)_{60}PVDF_{10}$ composites.

Figure 3a–e shows SEM images of the $S_{25}(CBhG)_{65}PVDF_{10}$ and $S_{25}FNPs_5(CBhG)_{60}PVDF_{10}$ composites. It is clear from Figure 3a–e that BTO, BFO, BNTFN, and BNTFC ferroelectric nanoparticles; carbon black; holey graphene; and sulfur were well mixed in the composites. The composite surface was smooth, which confirmed that the sulfur had dispersed in the hG framework very well. The holey graphene and CB acted as efficient electron transport carriers to ensure good electrical contact within the composites. The layered structures provided sufficient space to effectively absorb electrolytes, and buffering the volume expansion of the sulfur helped ensure sufficient electrochemical reactions and excellent cycling performance [46].

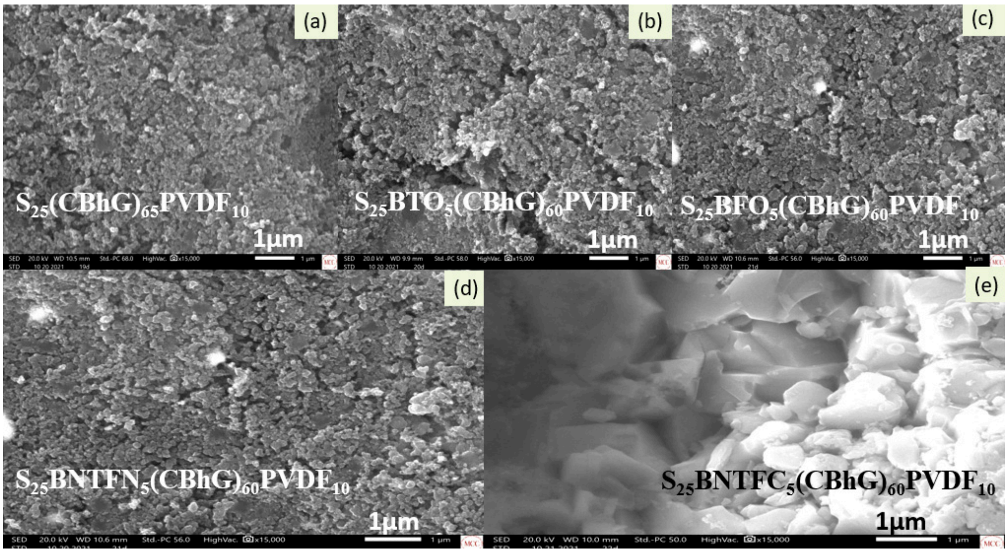

Figure 3. SEM images of (**a**) $S_{25}(CBhG)_{65}PVDF_{10}$, (**b**) $S_{25}BTO_5(CBhG)_{60}PVDF_{10}$, (**c**) $S_{25}BFO_5(CBhG)_{60}PVDF_{10}$, (**d**) $S_{25}BNTFN_5(CBhG)_{60}PVDF_{10}$, and (**e**) $S_{25}BNTFC_5(CBhG)_{60}PVDF_{10}$ composites with magnification of ×**15000** at 1 µm.

Figure 4 shows the EDS spectra of the $S_{25}(CBhG)_{65}PVDF_{10}$ and $S_{25}FNPs_5(CBhG)_{60}PVDF_{10}$ composites. In each spectrum, the S-peak was dominant due to its higher concentration relative to the carbon black, hG, PVDF, $BiFeO_3$, $BaTiO_3$, $Bi_4NdTi_3Fe_{0.7}Ni_{0.3}O_{15}$, and $Bi_4NdTi_3Fe_{0.5}Co_{0.5}O_{15}$, although the observed peaks clearly indicated their presence.

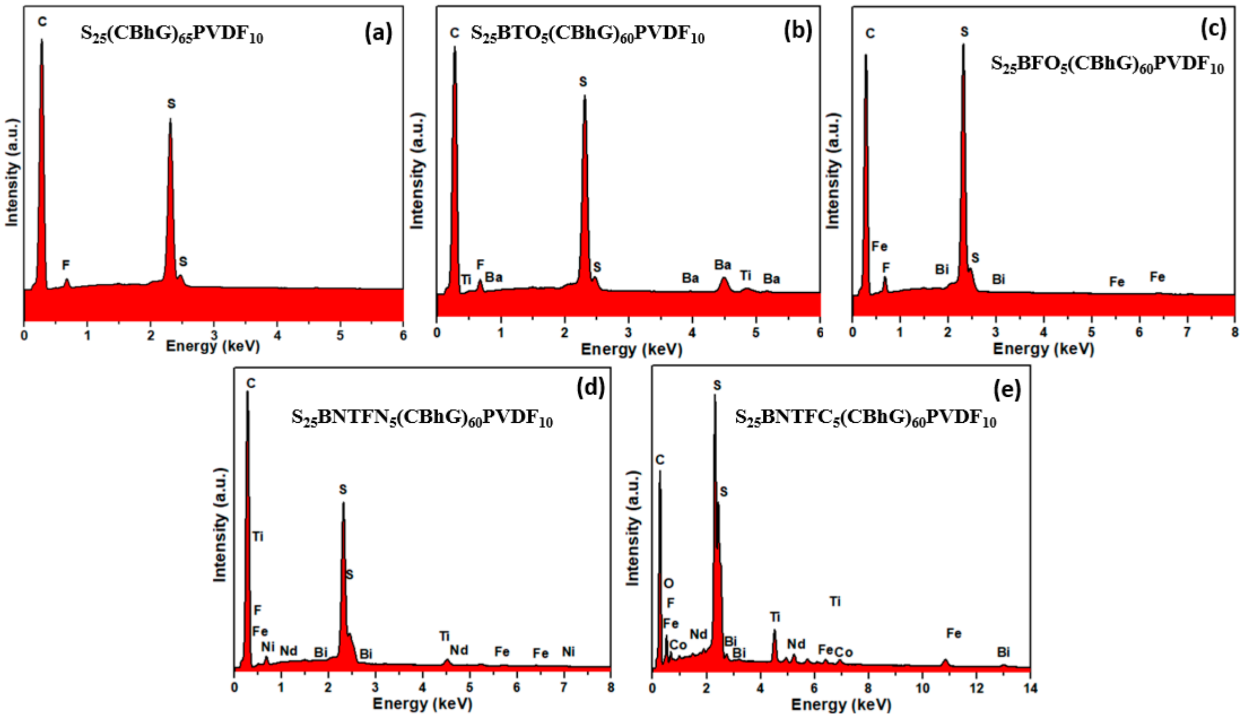

Figure 4. EDS of (**a**) $S_{25}(CBhG)_{65}PVDF_{10}$, (**b**) $S_{25}BTO_5(CBhG)_{60}PVDF_{10}$, (**c**) $S_{25}BFO_5(CBhG)_{60}PVDF_{10}$, (**d**) $S_{25}BNTFN_5(CBhG)_{60}PVDF_{10}$, and (**e**) $S_{25}BNTFC_5(CBhG)_{60}PVDF_{10}$ composites.

Figure 5 shows the Nyquist plots for the $S_{25}(CBhG)_{65}PVDF_{10}$, $S_{25}BTO_5(CBhG)_{60}PVDF_{10}$, $S_{25}BNTFN_5(CBhG)_{60}PVDF_{10}$, and $S_{25}BNTFC_5(CBhG)_{60}PVDF_{10}$ composites. The Nyquist plot of the $S_{25}BFO_5(CBhG)_{60}PVDF_{10}$ composite is shown in the inset for clarity. All the EIS spectra showed depressed semicircles in the high-frequency region, corresponding to the charge-transfer process, and a sloping straight line in the low-frequency region was consistent with the semi-infinite Warburg diffusion process [45,46].

The EIS spectra before charge-discharge for all batteries were fitted with an R(CR)W model and the results are shown in Table 3. It was observed that the charge-transfer resistance (R_{ct}) values for the $S_{25}FNPs5(CBhG)_{60}PVDF_{10}$ composites were higher than those for the pristine $S_{25}(CBhG)_{65}PVDF_{10}$ composite. The diffusion coefficients for samples with various FNPs were almost the same except for the BFO nanoparticles, which exhibited slightly higher values favoring good ionic conduction for lithium ions. The values of solution resistances (R_s) for FNP-doped composite cathodes varied between 11.08 Ω and 5.32 Ω. In comparison, the pristine $S_{25}(CBhG)_{65}PVDF_{10}$ composite exhibited a low solution resistance (R_s) of ~4.92 Ω and a low charge transference resistance of ~7.63 Ω. Rs reflected not only the electrolytic solution resistance but also a penetration or affinity of the solution within the cathode, anode, and separator. The higher Rs and R_{ct} for the BNTFN battery may have been due to the insufficient penetration or affinity of the solution within it [47]. The increase in R_s due to the cyclic charge–discharge processes might have been related to electrolyte degradation.

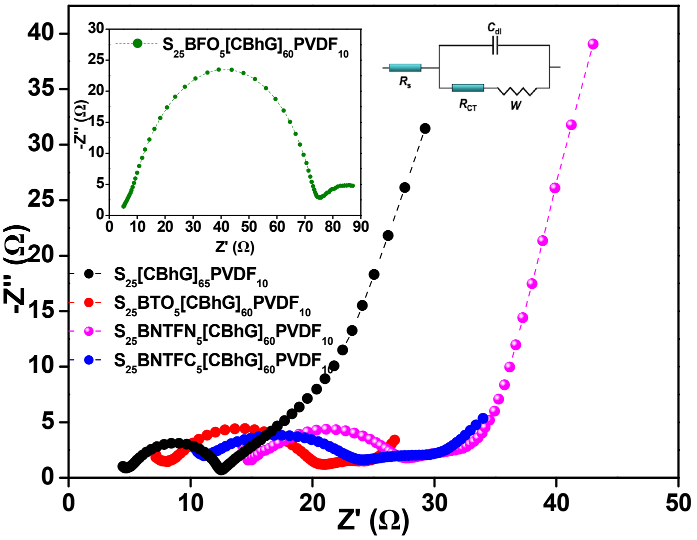

Figure 5. Nyquist plot comparison from electrochemical impedance spectroscopy spectrum measurements before charge-discharge of all battery cells with $S_{25}(CBhG)_{65}PVDF_{10}$, $S_{25}BTO_5(CBhG)_{60}PVDF_{10}$, $S_{25}BFO_5(CBhG)_{60}PVDF_{10}$ (inset), $S_{25}BNTFN_5(CBhG)_{60}$PVDF10, and $S_{25}BNTFC_5(CBhG)_{60}PVDF_{10}$ cathodes of studies from 1 MHz to 0.1 Hz at room temperature with circuit model.

Table 3. Interfacial characteristics calculated using EIS with R(CR)W model.

Electrodes	R_s [Ω]	C	R_{ct} [Ω]	W_{sc}	D_{li} [cm^2/s]
$\mathbf{S_{25}(CBhG)_{65}PVDF_{10}}$	4.92	0.027	7.63	0.0320	2.17×10^{-16}
$\mathbf{S_{25}BTO_5(CBhG)_{60}PVDF_{10}}$	8.15	1.459×10^{-8}	12.67	0.1438	3.43×10^{-15}
$\mathbf{S_{25}BFO_5(CBhG)_{60}PVDF_{10}}$	5.32	1.948×10^{-8}	69.77	0.0907	4.15×10^{-15}
$\mathbf{S_{25}BNTFN_5(CBhG)_{60}PVDF_{10}}$	14.85	0.179	12.82	0.0268	2.91×10^{-15}
$\mathbf{S_{25}BNTFC_5(CBhG)_{60}PVDF_{10}}$	11.08	1.234×10^{-8}	13.11	0.0705	4.11×10^{-15}

Figure 6 shows the charge–discharge profiles for the $S_{25}(CBhG)_{65}PVDF_{10}$ and $S_{25}FNPs_5$-$(CBhG)_{60}PVDF_{10}$ composite cathodes with varying fractions of FNPs. The $S_{25}(CBhG)_{65}PVDF_{10}$ cathode without FNPs provided an initial specific capacity of 1123 mAh/g_s at a current density of 0.2 mA/cm^2 and a reversible capacity of 541 mAh/g_s after 134 cycles at 0.3 mA/cm^2, as shown in Figure 6a,f. The specific capacity values of the $S_{25}BTO_5(CBhG)_{60}PVDF_{10}$ cathode for the 1st, 2nd, and 110th cycles were 1402, 1287, and 625 mAh/g_s, respectively, as shown in Figure 6b,g. The specific capacity values of the $S_{25}BFO_5(CBhG)_{60}PVDF_{10}$ cathode for the 1st, 2nd, and 116th cycles were 1430, 1325, and 564 mAh/g_s, respectively, as shown in Figure 6c,h. The specific capacity values of $S_{25}BNTFN_5(CBhG)_{60}PVDF_{10}$ for the 1st, 2nd, and 158th cycles were 1486, 1287, and 676 mAh/g_s, respectively, as shown in Figure 6d,i. The specific capacity values of the $S_{25}BNTFC_5(CBhG)_{60}PVDF_{10}$ cathode for the 1st, 2nd, and 107th cycles were 1509, 1350, and 505 mAh/g_s, respectively, as shown in Figure 6e,j. For all batteries, the current density was 0.2 mA/cm^2 for the first three cycles and 0.3 mA/cm^2 for the rest of the cycles. These remarkable values were attributed to the trapping of polysulfides through polar interactions with the FNP particles embedded in the cathodes [48]. The Coulombic efficiency values of the $S_{25}FNPs_5(CBhG)_{60}PVDF_{10}$ composite cathodes were in the range of 80–90%, as shown in Figure 6g–j, an improvement upon 67% for the composite cathodes without FNPs. This indicated that the modified composite cathodes had an improved reversible capacity. In Figure 6a–e, the initial discharge capacities of various $S_{25}FNPs_5(CBhG)_{60}PVDF_{10}$ composites values improved to 1400–1500 mAh/g_s, in comparison to 1123 mAh/g_s for the pristine $S_{25}(CBhG)_{65}PVDF_{10}$. The comparison of specific capacity, areal capacity, and capacity retention for the Li-S batteries is shown in Table 4.

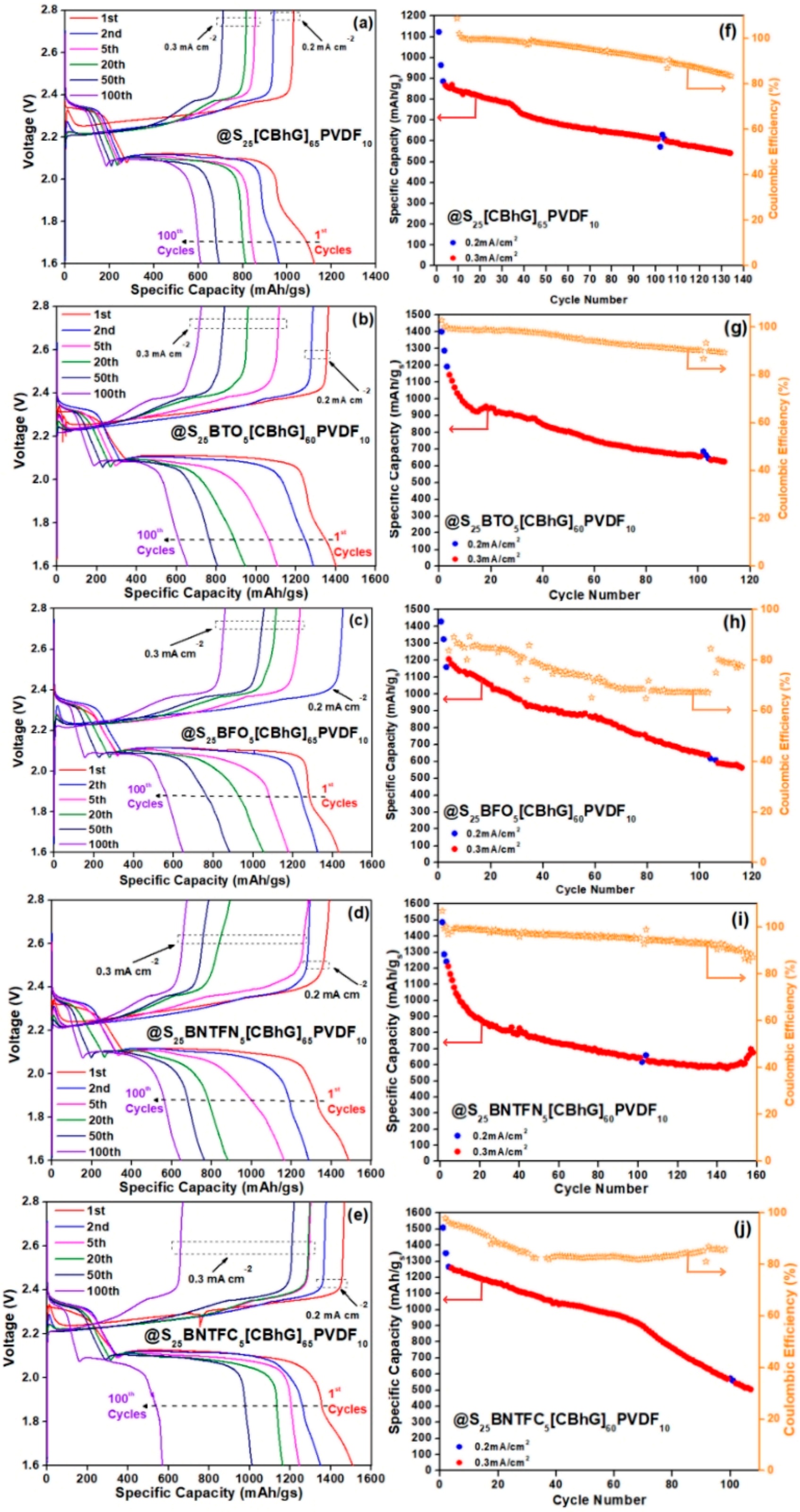

Figure 6. Charge-discharge profiles and specific capacity, Coulombic efficiency in function cycle number spectra of battery with $S_{25}(CBhG)_{65}PVDF_{10}$ at various current densities from 0.2 mA/cm^2 to 0.3 mA/cm^2 (**a**–**f**), battery with $S_{25}BTO_5(CBhG)_{60}PVDF_{10}$ (**b**–**g**), battery with $S_{25}BFO_5(CBhG)_{60}PVDF_{10}$ values (**c**–**h**), battery with $S_{25}BNTFN_5(CBhG)_{60}PVDF_{10}$ values (**d**–**i**), and battery with $S_{25}BNTFC_5(CBhG)_{60}PVDF_{10}$ values (**e**–**j**). All batteries were run over cycling at 0.2 mA/cm^2 (first 3 cycles were run at 0.3 mA/cm^2).

Table 4. Comparison of specific capacity [mAh/g_s] between 1st and 100th cycles, areal capacity for 1st cycle, and capacity retention for all batteries.

Electrodes	Specific. Cap. 1st Cyc. [mAh/g_s]	Specific. Cap. 100th Cyc. [mAh/g_s]	Areal Cap. 1st Cyc. [mAh/cm^{-2}]	Capacity Retention [%]
$S_{25}(CBhG)_{65}PVDF_{10}$	1123	612	4.84	54.49
$S_{25}BTO_5(CBhG)_{60}PVDF_{10}$	1402	655	5.08	46.72
$S_{25}BFO_5(CBhG)_{60}PVDF_{10}$	1430	648	5.60	45.31
$S_{25}BNTFN_5(CBhG)_{60}PVDF_{10}$	1486	645	5.12	43.40
$S_{25}BNTFC_5(CBhG)_{60}PVDF_{10}$	1509	572	6.74	37.90

Figure 7a represents three plateau regions in the charge–discharge profiles, which are typical characteristics of Li-S batteries. The formation of a valley at the end of the first discharge plateau and a peak at the beginning of the charging process could be observed in the curves during the transition of ions from solid to liquid. In comparison to $S_{25}(CBhG)_{65}PVDF_{10}$, $S_{25}BNTFC_5(CBhG)_{60}PVDF_{10}$ cathodes exhibited improved S utilization in terms of specific capacity (1123 mAh/g_s versus 1509 mAh/g_s), with mass loading (4.84 mg_s/cm^2 versus 6.74 mg_s/cm^2) and over potential ($\Delta E \sim 0.16$ V versus 0.17 V at the 2nd cycle), as shown in Figure 7a,b. Cycle performance testing (Figure 7b) was conducted to quantify the population of the battery, according to the requirements and life expectations of the battery for its various applications. With varying current densities, the discharge performance resulted in a two-way acceleration by means of increasing the battery degradation (capacity fade) rate and reducing the time required to complete one full charge-discharge cycle. Hence, it is very important to achieve a good cycling performance of the battery; it should thus be tested at various current densities for the accelerated use of Li-S batteries. To achieve high areal capacity, high mass loadings of 4.31 mg_s/cm^2, 3.625 mg_s/cm^2, 3.92 mg_s/cm^2, 3.45 mg_s/cm^2, and 4.46 mg_s/cm^2 were required. The highest initial discharge areal capacity reached > 6 mAh/cm^2.

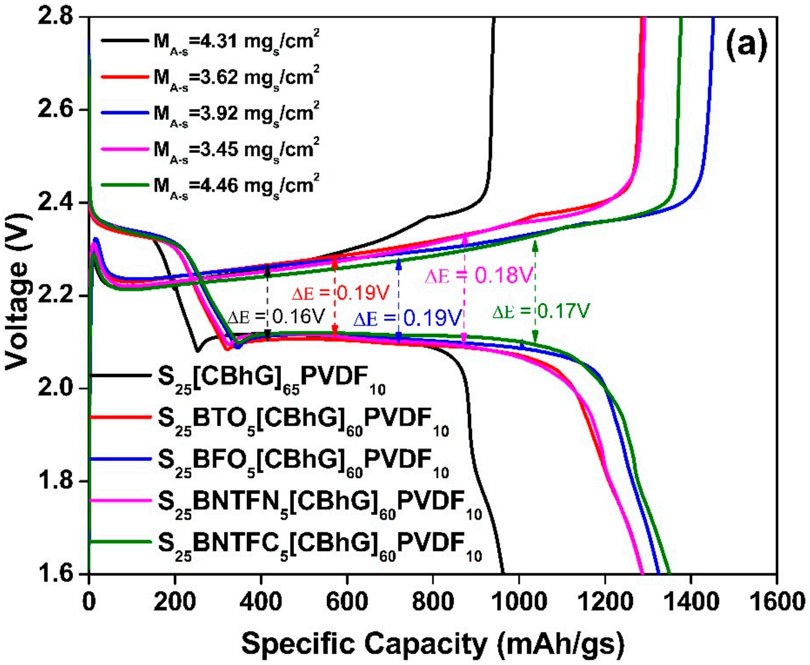

Figure 7. *Cont.*

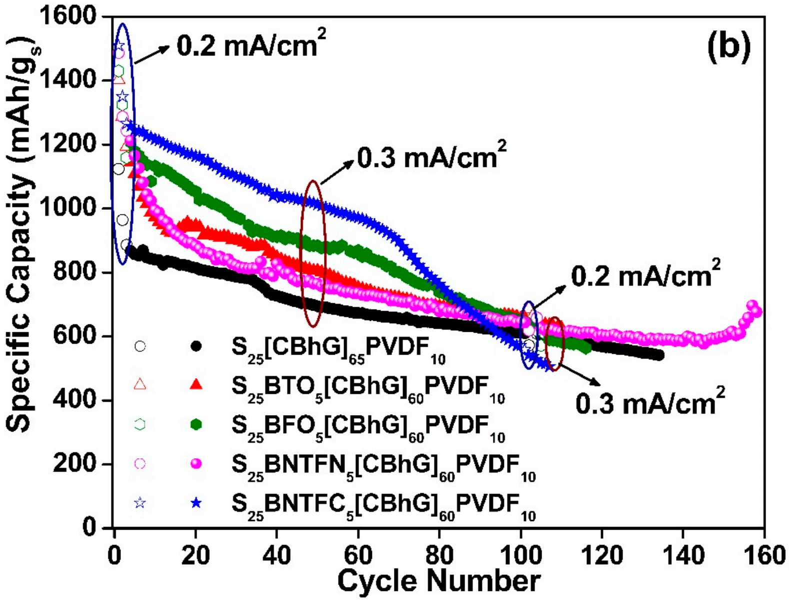

Figure 7. Comparison of electrochemical performance of $S_{25}(CBhG)_{65}PVDF_{10}$ and $S_{25}FNPs_5(CBhG)_{60}PVDF_{10}$ materials: (**a**) charge–discharge profile of 2 cycles for the batteries evaluated at current densities of 0.2 mA/cm^2, (**b**) specific capacity in function cycle number at current densities of 0.2 mA/cm^2 and 0.3 mA/cm^2.

Figure 8 shows that the values of areal capacity reached 4.84 mAh/cm^2, 5.08 mAh/cm^2, 5.60 mAh/cm^2, 5.12 mAh/cm^2, and 6.74 mAh/cm^2 for the $S_{25}(CBhG)_{65}PVDF_{10}$, $S_{25}BTO_5$-$(CBhG)_{60}PVDF_{10}$, $S_{25}BFO_5(CBhG)_{60}PVDF_{10}$, $S_{25}BNTFN_5(CBhG)_{60}PVDF_{10}$, and $S_{25}BNTFC_5$-$(CBhG)_{60}PVDF^{10}$ cathode composites, respectively. Among the investigated composites, the highest areal capacity was obtained for the $S_{25}BNTFC_5(CBhG)_{60}PVDF_{10}$ cathode [49].

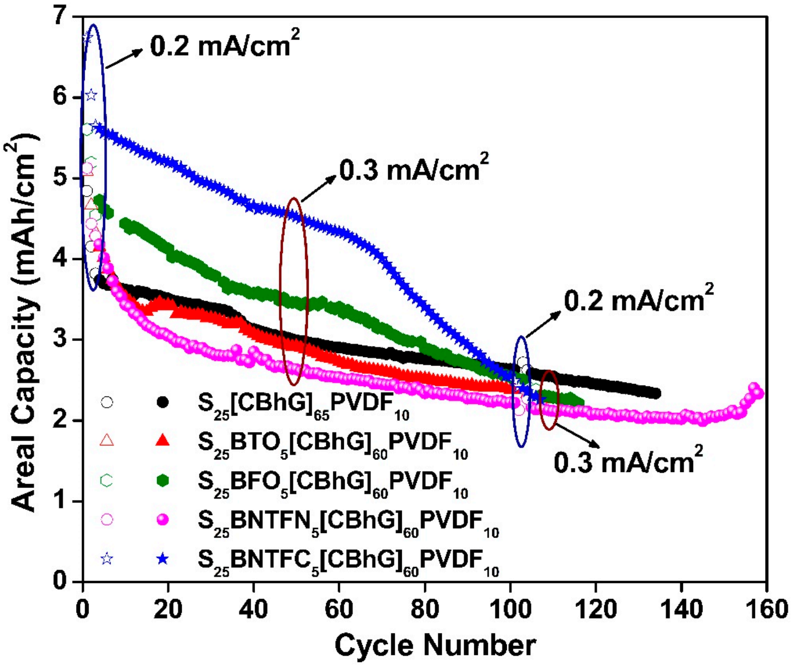

Figure 8. Areal capacity for the batteries evaluated at different current densities ran at 0.2 mA/cm^2 and 0.3 mA/cm^2. The composite cathodes are represented by black circles for $S_{25}(CBhG)_{65}PVDF_{10}$, red triangles for $S_{25}BTO_5(CBhG)_{60}PVDF_{10}$, green hexagons for $S_{25}BFO_5(CBhG)_{60}PVDF_{10}$, magenta circles for $S_{25}BNTFN_5(CBhG)_{60}PVDF_{10}$, and blue stars for $S_{25}BNTFC_5(CBhG)_{60}PVDF_{10}$.

4. Conclusions

In this work, sulfur composite cathodes were prepared, with hG as the dry pressable matrix and conductive scaffold. FNPs were added to improve electrochemical performance by reducing polysulfide shuttling. The Raman spectra confirmed the dominance of hG and the presence of FNPs in the composites, while SEM images confirmed the homogeneous distribution of FNPs throughout the composite matrix. EIS analysis confirmed the good diffusion of Li^+ ions during charge–discharge of the composite electrodes. The enhancement in diffusion coefficients due to the coupling of FNPs was attributed to the improvement in the rate performance of the composites. The electrochemical performance represents an innovative contribution to the development of high energy density and stable Li-S batteries. The significant improvement in the stability as well as the dramatic change in the cyclability of the Li-S batteries was attributed to the contribution of the bi-functional effect of ferroelectricity coupled with the hG/S composite system. When BNTFN nanoparticles were incorporated into the cathode's fabrication, the observed capacity at the first cycle was 1486 mAh/g_s, and after ~158 cycles, it was still high (~676 mAh/g_s). This also occurred with BNTFC, where the capacity started at ~1509 mAh/g_s, and after 100 cycles, had a value of ~500 mAh/g_s. The electrochemical performance retention of the fabricated electrodes up to 100 cycles showed a specific capacity (~541 mAh/g_s). The Coulombic efficiency improved by more than 10% upon adding ferroelectric nanoparticles into the composite cathode. The highest areal capacity value obtained for the composite electrodes was 6.74 mAh/cm^2. The incorporation of ferroelectric nanoparticles into the cathodes of Li-S batteries controlled the formation of polysulfides due to their internal electric fields, which reduced the rapid formation of polysulfides. This was attributed to the effect of an extra internal field induced by the ferroelectric nanoparticles. The development of such composite electrodes will provide good inspiration towards a strategy for suppressing the polysulfide shuttle phenomenon in the Li-S cell system and contribute to the advanced design of better Li-S cathodes for the next generation of energy storage systems.

Author Contributions: Conceptualization, C.C.Z.-G. and R.S.K.; methodology, C.C.Z.-G.; investigation, C.C.Z.-G., writing—original draft preparation, C.C.Z.-G.; writing—review and editing, B.T., R.K.K., C.O.P.-R.; M.C., R.S.K., D.K.P. and G.M.; supervision, M.C. and R.S.K.; funding acquisition, R.S.K. and G.M. All authors have read and agreed to the published version of the manuscript.

Funding: This research was funded by NASA MIRO PR-SPRInT, grant no. 80NSSC19M0236; NASA EPSCoR RID, grant no. 80NSSC19M0049; and NSF-EPSCoR Center for the Advancement of Wearable Technologies (CAWT) NSF, grant no. OIA-1849243.

Data Availability Statement: The data for this study are available from the corresponding authors upon request.

Acknowledgments: The authors are grateful for the financial support of NASA MIRO PR-SPRInT, grant no. 80NSSC19M0236; NASA EPSCoR, grant no. 80NSSC19M0049; and NSF-EPSCoR Center for the Advancement of Wearable Technologies (CAWT) NSF, grant no. OIA-1849243. We wish to express our gratitude to members of the SPECLAB group, especially William Pérez and the Molecular Science Research Center (MSRC) at the University of Puerto Rico, for the help and instruments provided during the experimental process and the fruitful discussions. We also thank Yi Lin from NASA Langley Research Center for providing the holey graphene material and for the fruitful discussions.

Conflicts of Interest: The authors declare no conflict of interest.

References

1. Manthiram, A.; Chung, S.-H.; Zu, C. Lithium-Sulfur Batteries: Progress and Prospects. *Adv. Mater.* **2015**, *27*, 1980–2006. [CrossRef] [PubMed]
2. Song, R.; Fang, R.; Wen, L.; Shi, Y.; Wang, S.; Li, F. A trilayer separator with dual function for high performance lithium–sulfur batteries. *J. Power Sources* **2016**, *301*, 179–186. [CrossRef]
3. Bruce, P.G.; Freunberger, S.A.; Hardwick, L.J.; Tarascon, J.-M. Li-O_2 and Li-S batteries with high energy storage. *Nat. Mater.* **2011**, *11*, 19–29. [CrossRef]

4. Fang, R.; Zhao, S.; Sun, Z.; Wang, D.-W.; Cheng, H.-M.; Li, F. More Reliable Lithium-Sulfur Batteries: Status, Solutions and Prospects. *Adv. Mater.* **2017**, *29*, 1606823. [CrossRef] [PubMed]
5. Lv, D.; Zheng, J.; Li, Q.; Xie, X.; Ferrara, S.; Nie, Z.; Mehdi, L.B.; Browning, N.D.; Zhang, J.-G.; Graff, G.L.; et al. High Energy Density Lithium-Sulfur Batteries: Challenges of Thick Sulfur Cathodes. *Adv. Energy Mater.* **2015**, *5*, 1402290. [CrossRef]
6. Seh, Z.W.; Sun, Y.; Zhang, Q.; Cui, Y. Designing high-energy lithium-sulfur batteries. *Chem. Soc. Rev.* **2016**, *45*, 5605–5634. [CrossRef]
7. Mikhaylik, Y.V.; Akridge, J.R. Polysulfide Shuttle Study in the Li-S Battery System. *J. Ofthe Electrochem. Soc.* **2004**, *151*, A1969–A1976. [CrossRef]
8. Zhou, G.; Li, L.; Wang, D.-W.; Shan, X.-Y.; Pei, S.; Li, F.; Cheng, H.-M. A flexible sulfur-graphene-polypropylene separator integrated electrode for advanced Li-S batteries. *Adv. Mater.* **2015**, *27*, 641–647. [CrossRef]
9. Liang, J.; Yin, L.; Tang, X.; Yang, H.; Yan, W.; Song, L.; Cheng, H.-M.; Li, F. Kinetically Enhanced Electrochemical Redox of Polysulfides on Polymeric Carbon Nitrides for Improved Lithium-Sulfur Batteries. *ACS Appl. Mater. Interfaces* **2016**, *8*, 25193–25201. [CrossRef]
10. Han, X.; Yang, Z.; Zhao, B.; Zhu, S.; Zhou, L.; Dai, J.; Kim, J.-W.; Liu, B.; Connell, J.W.; Li, T.; et al. Compressible, Dense, Three-Dimensional Holey Graphene Monolithic Architecture. *ACS Nano* **2017**, *11*, 3189–3197. [CrossRef]
11. Yen, Y.-J.; Chen, T.-H.; Wang, Y.-T.; Robles, A.; Đerić, M.; Miljanić, O.; Kaveevivitchai, W.; Chung, S.-H. Selective chemisorption of polysulfides by porous molecular crystal: Cathode host materials for lean-electrolyte lithium-sulfur cells with high electrochemical stability. *J. Power Sources* **2023**, *565*, 232891. [CrossRef]
12. Shah, S.S.; Aziz, A.; Cevik, E.; Ali, M.; Gunday, S.T.; Bozkurt, A.; Yamani, Z.H. Sulfur nano-confinement in hierarchically porous jute derived activated carbon towards high-performance supercapacitor: Experimental and theoretical insights. *J. Energy Storage* **2022**, *56*, 105944. [CrossRef]
13. Yan, S.-X.; Wang, Q.; Luo, S.-H.; Zhang, Y.-H.; Liu, X.; Liu, Y.-G.; Wang, Z.-Y.; Hao, A.-M.; Yi, T.-F. Coal-based S hybrid self-doped porous carbon for high-performance supercapacitors and potassium-ion batteries. *J. Power Sources* **2020**, *461*, 228151. [CrossRef]
14. Zhang, M.; Song, Z.; Liu, H.; Wang, A.; Shao, S. MoO_2 coated few layers of MoS_2 and FeS_2 nanoflower decorated S-doped graphene interoverlapped network for high-energy asymmetric supercapacitor. *J. Colloid Interface Sci.* **2021**, *584*, 418–428. [CrossRef] [PubMed]
15. Raj, F.R.M.S.; Jaya, N.V.; Boopathi, G.; Kalpana, D.; Pandurangan, A. S-doped activated mesoporous carbon derived from the Borassus flabellifer flower as active electrodes for supercapacitors. *Mater. Chem. Phys.* **2020**, *240*, 122151.
16. Gu, W.; Sevilla, M.; Magasinski, A.; Fuertes, A.B.; Yushin, G. Sulfur-containing activated carbons with greatly reduced content of bottle neck pores for double-layer capacitors: A case study for pseudocapacitance detection. *Energy Environ. Sci.* **2013**, *6*, 2465–2476. [CrossRef]
17. Cao, S.; Liu, D.; Ding, H.; Lu, H.; Gui, J. Towards understanding corrosion inhibition of sulfonate/carboxylate functionalized ionic liquids: An experimental and theoretical study. *J. Colloid Interface Sci.* **2020**, *579*, 315–329. [CrossRef]
18. Sahoo, R.K.; Singh, S.; Yun, J.M.; Kwon, S.H.; Kim, K.H. Sb_2S_3 Nanoparticles Anchored or Encapsulated by the Sulfur-Doped Carbon Sheet for High-Performance Supercapacitors. *ACS Appl. Mater. Interfaces* **2019**, *11*, 33966–33977. [CrossRef]
19. Wang, C.; Zhang, S.-H.; Zhang, L.; Xi, R.; Jiang, D.-P.; Chen, Z.-Y.; Huang, H.; Ding, L.-Y.; Pan, G.-B. Natural bamboo leaves derived sulphur-doped mesoporous heteroatom enriched carbon for high-performance supercapacitors and gas sensors. *J. Power Sources* **2019**, *443*, 227183. [CrossRef]
20. Zhou, Y.; Candelaria, S.L.; Liu, Q.; Huang, Y.; Uchaker, E.; CaO, G. Sulfur-rich carbon cryogels for supercapacitors with improved conductivity and wettability. *J. Mater. Chem. A* **2014**, *2*, 8472–8482. [CrossRef]
21. Ma, X.; Song, X.; Ning, G.; Hou, L.; Kan, Y.; Xiao, Z.; Li, W.; Ma, G.; Gao, J.; Li, Y. S-Doped Porous Graphene Microspheres with Individual Robust Red-Blood-Cell-Like Microarchitecture for Capacitive Energy Storage. *Ind. Eng. Chem. Res.* **2017**, *56*, 9524–9532. [CrossRef]
22. Salhabi, E.H.M.; Zhao, J.; Wang, J.; Yang, M.; Wang, B.; Wang, D. Hollow Multi-Shelled Structural $TiO_{2\text{-}x}$ with Multiple Spatial Confinement for Long-Life Lithium-Sulfur Batteries. *Angew. Chem. Int. Ed. Engl.* **2019**, *58*, 9078–9082. [CrossRef] [PubMed]
23. Song, J.; Yu, Z.; Gordin, M.L.; Wang, D. Advanced Sulfur Cathode Enabled by Highly Crumpled Nitrogen-Doped Graphene Sheets for High-Energy-Density Lithium-Sulfur Batteries. *Nano Lett.* **2016**, *16*, 864–870. [CrossRef] [PubMed]
24. Noheda, B.; Kooi, B.J. Ferroelectric chalcogenides—Materials at the edge. *Science* **2016**, *353*, 221–222.
25. Zhou, W.; Guo, B.; Gao, H.; Goodenough, J.B. Low-Cost Higher Loading of a Sulfur Cathode. *Adv. Energy Mater.* **2016**, *6*, 1502059. [CrossRef]
26. Ji, X.; Lee, K.T.; Nazar, L.F. A highly ordered nanostructured carbon-sulphur cathode for lithium-sulphur batteries. *Nat. Mater.* **2009**, *8*, 500–506. [CrossRef]
27. Xiao, J.; Wang, H.; Li, X.; Wang, Z.; Ma, J.; Zhao, H. N-doped carbon nanotubes as cathode material in Li–S batteries. *J. Mater. Sci. Mater. Electron.* **2015**, *26*, 7895–7900. [CrossRef]
28. Liu, T.; Zhang, L.; Cheng, B.; Hu, X.; Yu, J. Holey Graphene for Electrochemical Energy Storage. *Cell Rep. Phys. Sci.* **2020**, *1*, 100215. [CrossRef]
29. Yim, T.; Han, S.H.; Park, N.H.; Park, M.-S.; Lee, J.H.; Shin, J.; Choi, J.W.; Jung, Y.; Jo, Y.N.; Yu, J.-S.; et al. Effective Polysulfide Rejection by Dipole-Aligned $BaTiO_3$ Coated Separator in Lithium-Sulfur Batteries. *Adv. Funct. Mater.* **2016**, *26*, 7817–7823. [CrossRef]

30. Cheng, H.; Liu, H.; Jin, H.; Cai, N.; Gao, C.; Zhao, S.; Wang, M. Suppression of polysulfide shuttling with a separator modified using spontaneously polarized bismuth ferrite for high performance lithium–sulfur batteries. *J. Mater. Chem. A* **2020**, *8*, 16429–16436. [CrossRef]
31. Xie, K.; You, Y.; Yuan, K.; Lu, W.; Zhang, K.; Xu, F.; Ye, M.; Ke, S.; Shen, C.; Zeng, X.; et al. Ferroelectric-Enhanced Polysulfide Trapping for Lithium-Sulfur Battery Improvement. *Adv. Mater.* **2016**, *29*, 1604724. [CrossRef] [PubMed]
32. Zhao, Z.; Li, G.; Wang, Z.; Feng, M.; Sun, M.; Xue, X.; Liu, R.; Jia, H.; Wang, Z.; Zhang, W.; et al. Black $BaTiO_3$ as Multifunctional Sulfur Immobilizer for Superior Lithium Sulfur Batteries. *J. Power Sources* **2019**, *434*, 226729. [CrossRef]
33. Tripathi, B.; Katiyar, R.K.; Morell, G.; Dixit, A.; Katiyar, R.S. $BiFeO_3$ Coupled Polysulfide Trapping in C/S Composite Cathode Material for Li-S Batteries as Large Efficiency and High Rate Performance. *Energies* **2021**, *14*, 8362. [CrossRef]
34. Półrolniczak, P.; Walkowiak, M.; Kaźmierczak-Raźna, J.; Kasprzak, D.; Mathew, D.E.; Kathiresan, M.; Stephan, A.M.; Angulakshmi, N. $BaTiO_3$-g-GO as an efficient permselective material for lithium–sulfur batteries. *Mater. Chem. Front.* **2021**, *5*, 950–960. [CrossRef]
35. Zuluaga-Gómez, C.C.; Plaza-Rivera, C.O.; Tripathi, B.; Katiyar, R.K.; Pradhan, D.K.; Morell, G.; Lin, Y.; Correa, M.; Katiyar, R.S. Holey Graphene/Ferroelectric/Sulfur Composite Cathodes for HighCapacity Lithium–Sulfur Batteries. *ACS OMEGA* **2023**, *8*, 13097–13108. [CrossRef]
36. Lin, Y.; Han, X.; Campbell, C.J.; Kim, J.-W.; Zhao, B.; Luo, W.; Dai, J.; Hu, L.; Connell, J.W. Holey Graphene Nanomanufacturing: Structure, Composition, and Electrochemical Properties. *Adv. Funct. Mater.* **2015**, *25*, 2920–2927. [CrossRef]
37. Zhao, X.; Liu, W.; Chen, W.; Li, S. Preparation and properties of $BaTiO_3$ ceramics from the fine ceramic powder. *Ceram. Int.* **2015**, *41*, S111–S116. [CrossRef]
38. Bernardo, M.; Jardiel, T.; Peiteado, M.; Caballero, A.; Villegas, M. Reaction pathways in the solid state synthesis of multiferroic $BiFeO_3$. *J. Eur. Ceram. Soc.* **2011**, *31*, 3047–3053. [CrossRef]
39. Lin, Y.; Jones, K.J.; Greenburg, L.C.; Kim, J.-W.; Hu, L.; Connell, J.W. Facile, Solvent-Free Preparation of High Density, High Mass Loading Sulfur Cathodes Enabled by Dry-Pressable Holey Graphene Scaffolds. *Batter. Supercaps* **2019**, *2*, 774–783. [CrossRef]
40. Das, S.R.; Choudhary, R.N.P.; Bhattacharya, P.; Katiyar, R.S.; Dutta, P.; Manivannan, A.; Seehra, M.S. Structural and Multiferroic Properties of La-Modified $BiFeO_3$ Ceramics. *J. Appl. Phys.* **2007**, *101*, 034104. [CrossRef]
41. Chen, X.; Xiao, J.; Yao, J.; Kang, Z.; Yang, F.; Zeng, X. Room Temperature Magnetoelectric Coupling Study in Multiferroic $Bi_4NdTi_3Fe_{0.7}Ni_{0.3}O_{15}$ Prepared by a Multicalcination Procedure. *Ceram. Int.* **2014**, *40*, 6815–6819. [CrossRef]
42. Yang, F.J.; Su, P.; Wei, C.; Chen, X.Q.; Yang, C.P.; Cao, W.Q. Large Magnetic Response in $(Bi_4Nd)Ti_3(Fe_{0.5}Co_{0.5})O_{15}$ Ceramic at Room-Temperature. *J. Appl. Phys.* **2011**, *110*, 126102. [CrossRef]
43. Radhika, G.; Subadevi, R.; Krishnaveni, K.; Liu, W.R.; Sivakumar, M. Synthesis and Electrochemical Performance of PEG-$MnO_{(2)}$-Sulfur Composites Cathode Materials for Lithium-Sulfur Batteries. *J. Nanosci. Nanotechnol.* **2018**, *18*, 127–131. [CrossRef] [PubMed]
44. Li, M.; Zhang, Y.; Bai, Z.; Liu, W.W.; Liu, T.; Gim, J.; Jiang, G.; Yuan, Y.; Luo, D.; Feng, K.; et al. A Lithium-Sulfur Battery using a 2D Current Collector Architecture with a Large-Sized Sulfur Host Operated under High Areal Loading and Low E/S Ratio. *Adv. Mater.* **2018**, *30*, e1804271. [CrossRef]
45. Nguyen, T.Q.; Breitkopf, C. Determination of Diffusion Coefficients Using Impedance Spectroscopy Data. *J. Electrochem. Soc.* **2018**, *165*, E826–E831. [CrossRef]
46. Wang, T.; Zhang, Q.; Zhong, J.; Chen, M.; Deng, H.; Cao, J.; Wang, L.; Peng, L.; Zhu, J.; Lu, B. 3D Holey Graphene/Polyacrylonitrile Sulfur Composite Architecture for High Loading Lithium Sulfur Batteries. *Adv. Energy Mater.* **2021**, *11*, 2100448. [CrossRef]
47. Gaberscek, M. Understanding Li-based battery materials via electrochemical impedance spectroscopy. *Nat. Commun.* **2021**, *12*, 6513. [CrossRef] [PubMed]
48. Rana, M.; Ahad, S.A.; Li, M.; Luo, B.; Wang, L.; Gentle, I.; Knibbe, R. Review on areal capacities and long-term cycling performances of lithium sulfur battery at high sulfur loading. *Energy Storage Mater.* **2019**, *18*, 289–310. [CrossRef]
49. Fan, C.-Y.; Yuan, H.-Y.; Li, H.-H.; Wang, H.-F.; Li, W.-L.; Sun, H.-Z.; Wu, X.-L.; Zhang, J.-P. The Effective Design of a Polysulfide-Trapped Separator at the Molecular Level for High Energy Density Li-S Batteries. *ACS Appl Mater Interfaces* **2016**, *8*, 16108–16115. [CrossRef] [PubMed]